High Energy Density Physics 23 (2017) 73–80

Contents lists available at ScienceDirect

High Energy Density Physics

journal homepage: www.elsevier.com/locate/hedp

# A plasma deflagration accelerator as a platform for laboratory astrophysics

Thomas C. Underwood*, Keith T.K. Loebner, Mark A. Cappelli

*High Temperature Gasdynamics Laboratory, Stanford University, Stanford, California 94305, USA*

ARTICLE INFO

*Article History:*
Received 26 September 2016
Revised 27 February 2017
Accepted 2 March 2017
Available online 6 March 2017

*Keywords:*
Laboratory astrophysics
Astrophysical jets
Scaling laws
Magnetohydrodynamics (MHD)

ABSTRACT

The replication of astrophysical flows in the laboratory is critical for isolating particular phenomena and dynamics that appear in complex, highly-coupled natural systems. In particular, plasma jets are observed in astrophysical contexts at a variety of scales, typically at high magnetic Reynolds number and driven by internal currents. In this paper, we present detailed measurements of the plasma parameters within deflagration-produced plasma jets, the scaling of these parameters against both machine operating conditions and the corresponding astrophysical phenomena. Using optical and spectroscopic diagnostics, including Schlieren cinematography, we demonstrate the production of current-driven plasma jets of ~100 km/s and magnetic Reynolds numbers of ~100, and discuss the dynamics of their acceleration into vacuum. The results of this study will contribute to the reproduction of various types of astrophysical jets in the laboratory and indicate the ability to further probe active research areas such as jet collimation, stability, and interaction.



## 1. Introduction

Astrophysical plasma jets are ubiquitous throughout the universe, occurring in environments such as planetary nebulae, active galactic nuclei, and young stellar objects. Many of the jets arising from these sources achieve high velocities, $v \sim 100-300$ km/s, while still maintaining remarkable collimation over vastly different timescales [1,2]. For example, planetary nebulae have been observed to produce periodic jets with characteristic timescales around 1000 years where as Herbig–Haro objects yield outflows lasting up to $10^5$ years. In terms of spatial evolution, the majority of jets are fractions of parsecs in length and feature large length-to-width ratios indicating they remain narrow as the jets propagate over vast spatial scales [3]. Even with the ubiquitous nature and contemporary interest in plasma jets, there is still little known about the formation dynamics, role of instabilities, and the nature of interactions with their respective backgrounds.

Many of the remaining unknowns in astrophysical systems are driven not only by the complexity of the environments but also the vast disparity in scales involved. When also considering the enormous distances such objects are from Earth, it comes with little surprise that many astrophysical data sets are limited in their spatial, temporal, and even spectroscopic resolution. Laboratory experiments overcome much of these shortcomings by offering a repeatable, high resolution platform that can be used to complement astrophysical observations and numerical simulations. Although the benefits of superior repeatability and access are apparent for laboratory experiments, it is still a challenge to ensure that a *similarity* is maintained to relevant astrophysical systems. Without such similarity, there is no guarantee that predictions made regarding the behavior of laboratory experiments will hold when scaled larger systems. The most direct way of ensuring this similarity is by achieving the exact astrophysical conditions in the laboratory. For situations where this is not possible, similarity is still maintained when quantities of interest (such as pressure, density, space, time, etc.) can be mapped between the systems via multiplicative constants. With the advent of high energy devices (lasers, fast z-pinches), it has become possible over recent years to produce and study hypersonic jets in the laboratory setting [4,5]. Using such facilities as the OMEGA laser, recent work [6] has produced and studied the interaction of jets with ambient media leading to the formation of bow shocks. Other research [7,8] has utilized fast z-pinches in the form of a conical array of fine exploding wires to produce radiatively cooled hypersonic jets. Although scaled jets with impressive velocities and densities can be produced with such devices, there is significant research [9–11] that points to the jet's magnetic field, associated electric current, and lifetime as important metrics when trying to emulate the structure and dynamics of astrophysical flows.

In this work we present detailed experimental measurements of a plasma deflagration accelerator to gauge its ability to produce scaled astrophysical jets. The experiment and resulting flows

* Corresponding author.
*E-mail address:* tunderw5@stanford.edu (T.C. Underwood).

http://dx.doi.org/10.1016/j.hedp.2017.03.004
1574-1818/

detailed in this paper provide a unique combination of being completely driven by internal current and boast added stabilization mechanisms that result in jets lasting much longer that conventional pinch schemes. In Section 2 of this paper the physics and unique features of the plasma deflagration accelerator are discussed. Section 3 presents a comprehensive characterization of the device by discussing the experimental setup and resulting data. Finally, Section 4 combines the data detailed in Section 3 into relevant dimensionless groups and discusses how these numbers relate to astrophysical systems.

## 2. Plasma deflagration accelerator

The plasma source employed as a part of this work is a pulsed Lorentz force accelerator that is an extension of the classic Marshall plasma gun [12]. The device, as shown schematically in Fig. 1, features a coaxial rod configuration which has been used extensively in past studies for a variety of applications [13–16]. In terms of geometry, the entire accelerator region is 26 cm long, 5 cm in diameter and features a set of stainless steel rod anodes and a single central copper cathode. To ensure consistent and reliable performance, the accelerator is connected to a vacuum chamber that is maintained at $10^{-7}$ Torr between firing events.

The production of plasma jets first requires charged high voltage capacitors to be connected between the rod electrodes. A 56 μF capacitor bank was used throughout this study with charging voltages ranging from 3 to 9 kV. Given the accelerator is initially under high vacuum conditions, the anodes float at high voltage until a breakdown path occurs. To provide that, a fast rise-rate, variable mass-bit gas puff valve, detailed in [17], is used to inject neutral gas to the device upstream of the electrodes continuously during the firing process. Typically for the operating conditions considered in this paper, hydrogen gas is injected for ~1 ms where as the energy transfer and thus plasma dynamics occur over 20 μs. As the neutral gas accelerates in vacuum, it is ionized by the applied electric field resulting in a net radial current flow inward toward the cathode (as depicted by the blue arrows in Fig. 1). As this current is collected by the copper cathode and travels out of the system, an azimuthal B-field is produced. As a result of both the current flow and induced B-field, a strong $\boldsymbol{J} \times \boldsymbol{B}$ force accelerates the quasineutral plasma to high velocities.

As the plasma jet moves along the length of the accelerator, the $\boldsymbol{J} \times \boldsymbol{B}$ force remains the primary source of axial acceleration until the field topology changes near the end of the electrodes. At this point, the behavior of the device is strongly dependent on the operating mode of the accelerator. Previous work [18] has focused on understanding these modes and specifically investigating the transition of the device between the so-called delfagration and detonation or snowplow mode. For the geometry and operating parameters considered in this paper, the deflagration mode occurs for the first ~10 μs of the capacitor discharging process after which a transition occurs. For astrophysical applications, it is this delfagration mode that is of interest as it produces collimated, high-density jets.

As detailed in Fig. 1, the deflagration mode ensures the production of such jets by creating a radial compression in the form of a pinch. This pinch is produced because near the end of the accelerator volume, the current streamlines are still forced to terminate at the cathode which cause a radially directed $\boldsymbol{J} \times \boldsymbol{B}$ force. The remaining structure and dynamics of the jet are determined by the current convected downstream by the plasma in addition to the associated conversion of magnetic pressure to kinetic energy. One of the unique features of this device is the comparatively long lifetime of the jet. Research points to the shear flow [19] around the pinch as a stabilization mechanism against inherent instabilities that limit its lifetime.

## 3. Experimental characterization

Separate measurements of plasma density, velocity, and the resulting pinch structure were made to better understand the inherent properties of the plasma jet. These specific properties along with calculations of both the plasma temperature and magnetic field were determined to be critical parameters in deciding whether or not there may be relevant similarity to astrophysical flows.

### 3.1. Plasma density

Plasma density was measured at the exit plane of the deflagration accelerator, operating on hydrogen, where a maximum in optical emission and pinch dynamics have previously been observed [20]. To quantify the density, Stark broadening of the $n = 3$ to $n = 2$ hydrogen Balmer-alpha ($H\alpha$) electronic transition at 656.28 nm was measured using the configuration detailed in Fig. 2. Light was collected and focused on the entrance slit of a 0.75 m Spex 750 M spectrometer. Within this spectrometer, a 1200 groove/mm grating, blazed at $5^{\circ}10'$, was used to disperse the light and tune the output window to be centered around 656.28 nm. The light leaving the system was recorded using a Princeton instruments intensified CCD camera that was triggered coincidentally with the breakdown of the gas and featured a gate window of 10 μs to capture the entire deflagration event. The wavelength calibration factor (0.125 Å/pixel) and height calibration factor (0.16 mm/pixel) of the system were determined by placing a mercury lamp at the location of the plasma jet. Finally, the instrument broadening of the system was determined and eventually deconvolved from the measured Stark broadening using a hydrogen lamp.

An Abel transform was employed to convert the raw chord integrated intensity profiles to radially resolved plasma density. This

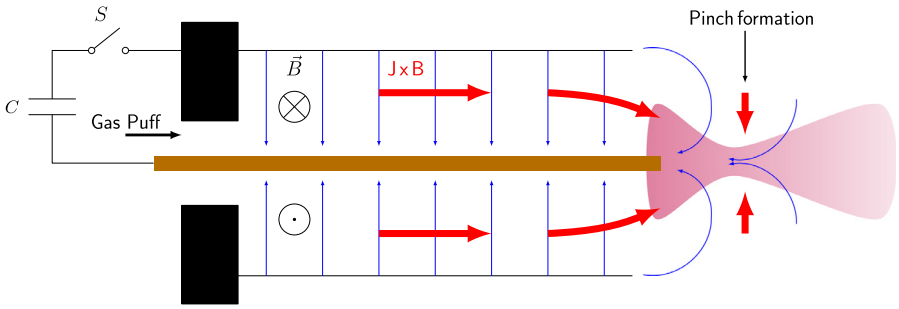


**Fig. 1.** Schematic detailing the underlying physics involved with the coaxial plasma deflagration accelerator operating in deflagration mode. Unique features of this device include its internally generated magnetic field and shear flow stabilization. In the diagram, blue arrows represent current conduction pathways (from anode to cathode via neutral gas ionization) which produce a resulting $\boldsymbol{B}$ where as the red arrows indicate the direction of the $\boldsymbol{J} \times \boldsymbol{B}$ force. (For interpretation of the references to colour in this figure legend, the reader is referred to the web version of this article.)

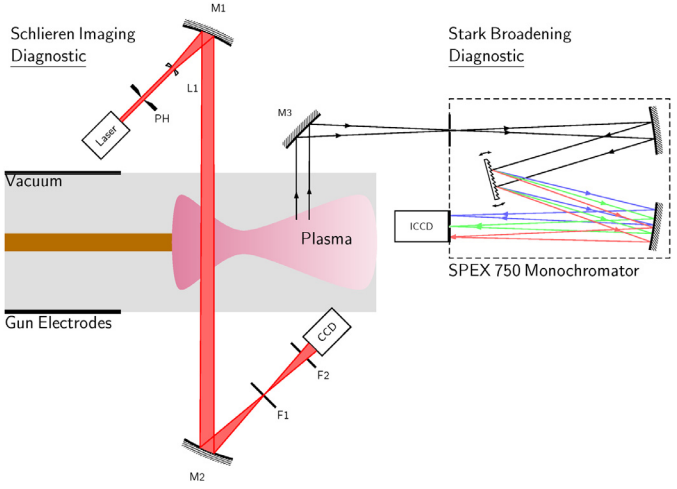


**Fig. 2.** Experimental setup used for measuring the plasma jet density, velocity, and pinch structure. The plasma density was measured by collecting optical emission from the jet, passing it through a spectrometer, and measuring its line broadening. The pinch structure was measured using a z-type Schlieren imaging setup with laser back-lighting. Finally the jet velocity was measured using the Schlieren imaging setup with no F1 or F2 filters and no laser back-lighting to only record a time-resolved video of optical emission. PH: Pinhole, L1: Beam expanding lens, M1, M2, M3: Mirrors, F1: Sooted slide gradient filter, F2: Laser line filter.

inversion process can be expressed mathematically according to,

$$\epsilon(r) = -\frac{1}{\pi}\int_r^R \frac{dI(y)}{dy}\frac{dy}{\sqrt{y^2-r^2}}, \tag{1}$$

where $I(y)$ is the measured chord-integrated intensity, $\epsilon(r)$ is the radially resolved emissivity, and $R$ is the radius at which the measured intensity reaches background levels. A number of different methods have been historically employed to evaluate Eq. (1) ranging from direct numerical integration to Fourier series representation. We chose to utilize the Nestor-Olsen method, given as,

$$\epsilon(r_k) = -\frac{2}{\pi\Delta y}\sum_{n-k}^{N-1} I(y_n)B_{k,n}, \tag{2}$$

where $\Delta y$ is the physical distance between adjacent pixels and $k/n$ are the indices representing position in the radial and vertical profiles respectively. The values for the weighting coefficients $B_{k,\ n}$ required for the evaluation of Eq. (2) can be found in Ref. [21].

One other important consideration is to determine the radial symmetry of the measured intensity profile. As the Abel inversion process implicitly makes a symmetry assumption, it is very sensitive to any structural anisotropies within the data. To get around the limitation, the raw Stark broadened Hα line, as shown in Fig. 3, was symmetrized around its centroid. The upper and lower left quadrants were not considered due to the frequent smearing of the Hα line with neighboring Fe impurity lines. Once symmetrized, the spectra was broken into individual vertical slices (each at a different $\lambda$), fit with a Gaussian function for smoothing purposes and inverted. A complete $\epsilon(\lambda, r)$ was then generated for each vertical slice. This data was then taken, broken into radial slices, and fit with a Voigt profile. As the Lorentzian component of the Voigt function is dominated by Stark broadening for the Hα line, this component was isolated from the fit after instrument broadening was removed, and used to calculate the plasma density via empirical correlations [22].

Representative time-averaged plasma density, $n(r)$, profiles over 10 μs obtained for capacitor charging voltage conditions ranging from 3 to 9 kV are detailed in Fig. 4a. The curves shown at negative radii are derived from data incorporated into the symmetrization procedure from the lower-righthand (LR) quadrant where as the data at positive radii originate from the upper-righthand (UR) quadrant (for the same trial). The peak data and radial structure of the two profiles are slightly different due to the sensitivity of the inversion process, however, given both the LR and UR profiles are completely independent, their variation compared to the structure

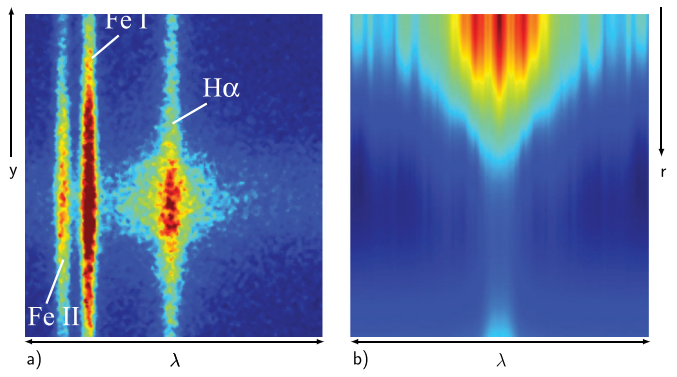


**Fig. 3.** (a) Example of a chord integrated intensity profile captured with the PI-MAX camera, $I(\lambda, y)$, as a function of vertical height, $y$, and wavelength, $\lambda$. (b) Resulting Abel-inverted emissivity profile as a function of radius and wavelength, $\epsilon(r, \lambda)$.

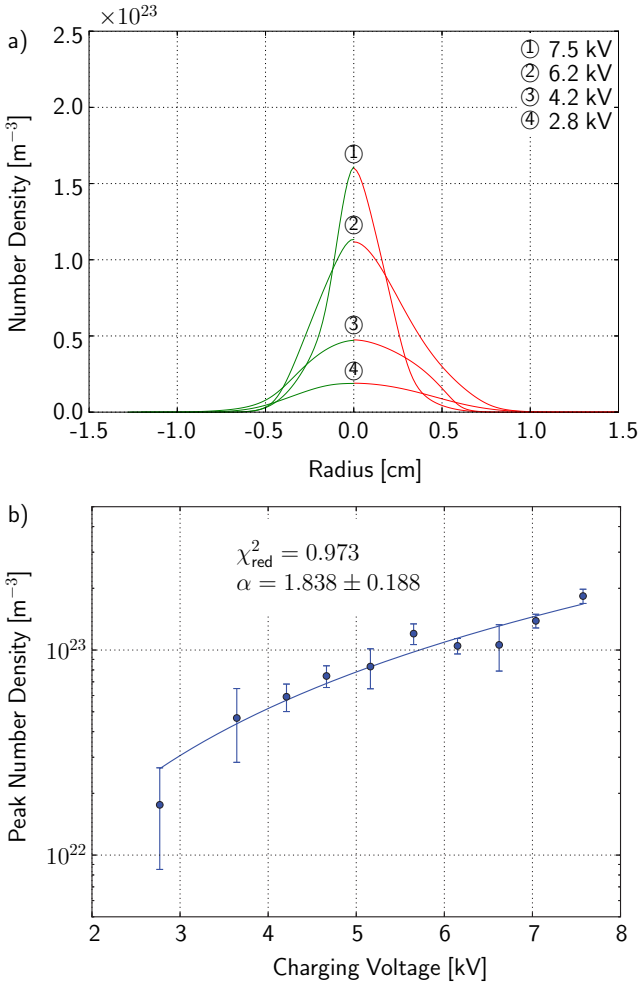


**Fig. 4.** (a) Selected plasma density radial profiles derived from measured intensity profiles. The green and red curves are derived from different quadrants of the intensity profile detailed in Fig. 3(a). (b) Scaling law of peak plasma density as a function of charging voltage. As $V \propto I$ for the device, data indicates that $n_e \propto V^{\alpha} \propto I^{\alpha}$. (For interpretation of the references to colour in this figure legend, the reader is referred to the web version of this article.)

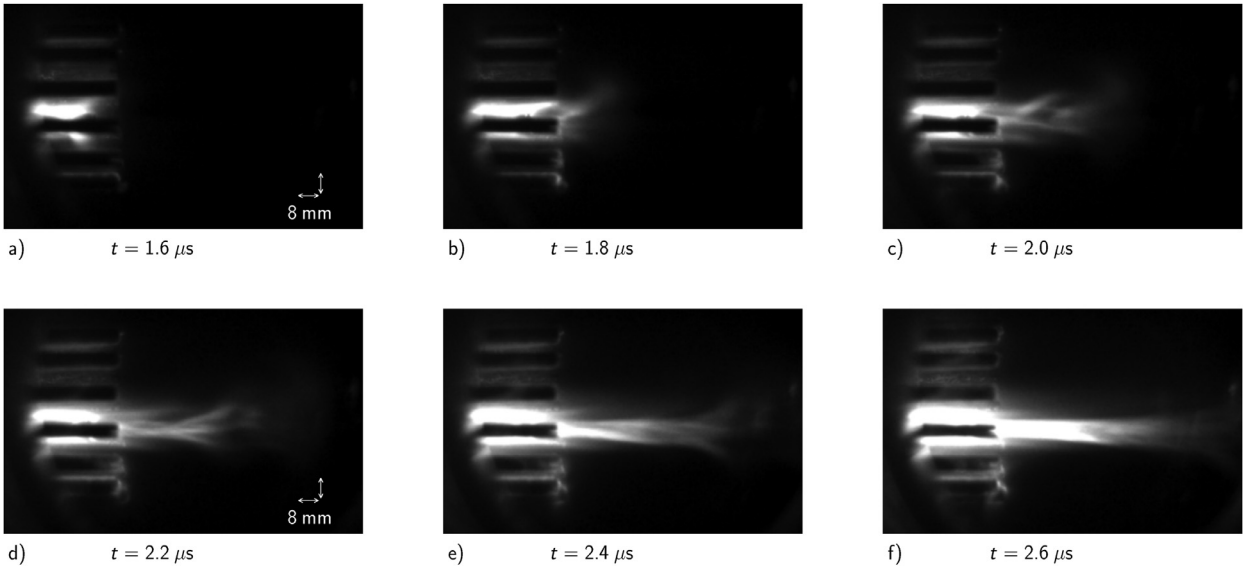


**Fig. 5.** Selected time resolved images of the early formation stages of the plasma deflagration event for a capacitor charging voltage of 9 kV. These images are a view of broadband plasma self-emission and are used to estimate jet velocity in Fig. 6.

of the underlying data clearly indicate the radial symmetry assumption of the jet is justified.

The empirical scaling law measured for the peak density variation as a function of charging voltage is detailed in Fig. 4b. The uncertainty in this plot was estimated by taking an average of 10 trials for each operating condition considered for the device. The final error estimate is a combination of shot-to-shot variability in addition to uncertainty caused by differences in peak density between the LR and UR profiles. For a function of the form $V^{\alpha}$, a best fit parameter of $\alpha = 1.838 \pm 0.188$ was found. Over all operating conditions of the device, it was found that the discharge current is linearly proportional to the charging voltage, thus the power law can also be expressed as $\sim I^2$. The fitting parameter is therefore consistent with a scaling law proportional to the magnetic pressure of the system or $B^2$.

### 3.2. Jet velocity

The plasma deflagration velocity was estimated using a time of flight method where the position of the jet's leading edge was tracked as a function of time. To achieve this, a high frame rate Shimadzu HPV-X2 CCD camera was employed and setup in the configuration detailed in Fig. 2. Both the laser backlight and gradient filters required for Schlieren imaging were removed to allow an unobstructed view of broadband plasma self-emission. The Shimadzu camera utilized in this work featured 50 ns exposure times and a 100 ns inter-frame time allowing a total of ~100 frames to investigate jet dynamics. Unlike other studies where a questionable assumption of experimental repeatability must be assumed due to device limitations, this camera allowed a complete time-resolved video of each individual trial. A neutral density filter with optical density, $d = 2$, was used to ensure the CCD camera was not saturated during discharge events. To illustrate the higher end of the velocities achievable with the device, a capacitor charging voltage of 9 kV was selected for this component of the study.

Of the ~100 images of the jet, a small subset were identified at early times in the deflagration event where the interface between the plasma and vacuum was clearly visible. A total of six of these images are detailed in Fig. 5. It is clear from these emission images that many of the structural features of astrophyscial flows, namely, high-velocity and collimation are produced from the accelerator. To estimate velocity from these emission snapshots, an edge tracking algorithm was used to identify the position within each image of the plasma-vacuum interface. Using the spatial calibration determined for the plasma self-emission optical system, 0.36 mm/pixel, a mapping of position as a function of time was found and is shown in Fig. 6. A resulting jet velocity of $V = 109 \pm 1$ km/s was found via the slope of the resulting line. Reported uncertainties in this number were due to both spread in the identified plasma-vacuum edge and structural variations observed within the jet from frame to frame.

### 3.3. Pinch characteristics

Although optical emission itself provides detailed information about plasma dynamics, the fact that it depends on $n^2$ makes it less attractive for resolving fine spatial structures. Schlieren imaging was used instead for uncovering the dynamics and structure of the pinch region because its signal is directly proportional to the gradient in density. Although Schlieren and other refractometry based methods

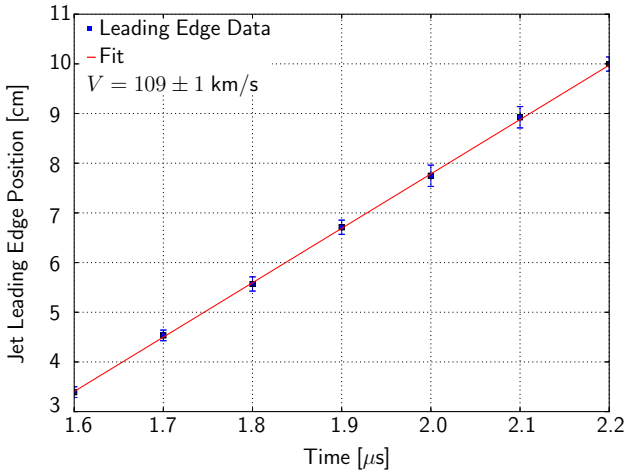


**Fig. 6.** Plot of plasma jet leading edge as a function of time for a capacitor charging voltage of 9 kV. A corresponding velocity of $V = 109 \pm 1$ km/s was found via the slope of the resulting fit.

have been used to visualize flow fields of countless experiments, great care was taken in the design of our optical setup. When attempting to image dense plasmas in particular, it is mandatory that the source of collimated light completely dominate any self-emission over the timescales relevant to flows of interest. A 637 nm, 250 mW diode laser was used to satisfy this constraint and ensure a signal to noise ratio, SNR, of 100 or more was achieved even during periods of the greatest optical emission.

A z-type Schlieren configuration was used featuring two 15.2 cm diameter $f/4$ mirrors, as shown in Fig. 2, as the system inherently minimizes coma and other optical aberrations. The use of a laser as a background source also added significant diffraction and artifacting effects to the Schlieren signal. Thus, as documented in Ref. [23], the standard knife-edge was replaced with a sooted slide. The soot was uniformly deposited on a glass slide with a flame to remove any hard edges that lead to diffractive effects. A plano-concave lens was added to the optical setup to expand the laser beam such that it was able to visualize the entirety of the accelerator exit plane. To further improve stray light rejection, a 635 nm laser line filter with a 10 nm bandpass was added to the optical system. As with the optical emission configuration, a Shimadzu HPV-X2 camera was employed featuring 50 ns exposure times and a 100 ns inter frame time which allowed a time-resolved video to be generated for each operating condition.

The spatial structure of the deflagration jet was investigated for two different capacitor charging conditions, namely, 5 kV and 9 kV. Unlike the time-average density measurements, which can also theoretically be used to obtain spatial properties of the jet, a unique advantage of the Schlieren configuration in this paper is the ability for the diagnostic to capture transient structures and instabilities of the plasma. In this study, the Schlieren diagnostic was used to identify gradient length scales within the jet and specific estimates of its total length and radius. The measurements of critical length scales for the accelerator are essential for evaluating dimensionless parameters relevant to astrophysical flows. Fig. 7 illustrates still images of the plasma jet 11 μs after breakdown once the essential features of the pinch have been established. Using the spatial calibration of the system, 0.23 mm/pixel, a minimum pinch radius of 5.3 mm and 3.6 mm was found for the 5 kV and 9 kV trials respectively while a jet length of more than 56 mm was found for both. It was also found that both the pinch radius and associated jet collimation were strong functions of the charging voltage of the capacitors and thus device current. As the induced magnetic field is a critical parameter in determining the pinch properties, the conclusion that the pinch become narrower as the current flow and thus magnetic field/pressure increased is consistent with expectations.

An equilibrium pinch model was used to determine the remaining critical features of the jet, namely magnetic field and temperature. Significant prior work [24] has been done that conclude the equilibrium profile predicted for the classic imploding z-pinch and shear-stabilized pinch, as in the deflagration accelerator, are the same. Such a model, in conjunction with the Stark-broadened density and pinch current, $I_p$, profiles allow estimates of spatially dependent parameters with the aid of empirical parameters.

A constant drift velocity model was applied to fully close the equilibrium pinch model. This amounts to assuming the current density is proportional to the measured number density, $j = Cn$. The proportionality constant, $C$, can be determined from both $n$ and $I_p$ according to,

$$C = \frac{I_p}{\int_0^{2\pi}\int_0^a n(r) r \, dr d\theta}, \tag{3}$$

where $a$ is the radius of the pinch. Noting the form of the current density, the azimuthal B-field can be determined via Ampere's Law,

$$B_\theta(r) = \frac{\mu_0}{r}\int_0^r j(r')r' dr'. \tag{4}$$

In the absence of an applied axial field, the momentum equation yields the equilibrium profile for a radial pinch,

$$\frac{dp}{dr} = -\frac{B_\theta(r)}{\mu_0 r}\frac{d}{dr}[rB_\theta(r)], \tag{5}$$

which can be solved to yield the pressure profile, $p(r)$. Finally combining this with the density profile and utilizing the ideal gas law, the temperature profile becomes,

$$T(r) = \frac{p(r)}{(1+1/Z)n(r)k_b}, \tag{6}$$

where $Z$ is the ionization state of the bulk plasma ions ($Z = 1$ for hydrogen).

The evaluation of Eqs. (3)–(6) requires explicit knowledge of both $n(r)$ and $I_p$. As with the jet velocity measurement, the peak jet parameters attainable over our operating range are of particular interest. Thus calculations were carried out for capacitor charging voltages of 5 kV and 9 kV. The density profile required for Eq. (3) was obtained from the Stark-broadening spatial profiles detailed in Fig. 4. The device current was measured by placing a wide-band current transformer around the transmission lines connecting the

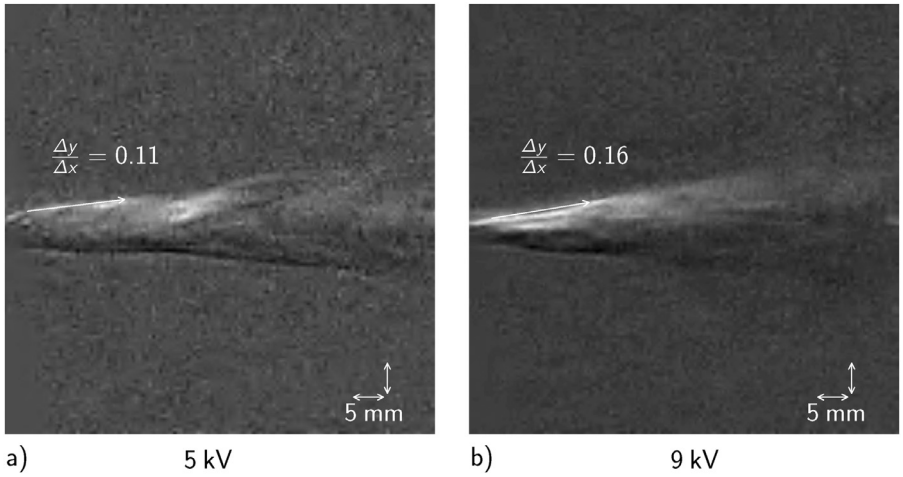


**Fig. 7.** Schlieren images of the plasma jet 11 μs after initial gas breakdown for (a) 5 kV and (b) 9 kV capacitor charging conditions. Both the pinch radius and jet collimation were observed to be strong functions of charging voltage.

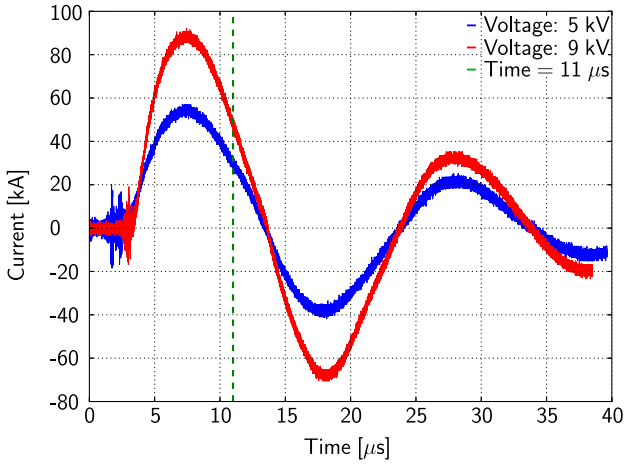


**Fig. 8.** Plot of the measured current being fed into the device from discharging capacitors at both 5 kV and 9 kV charging voltages as a function of time. The waveform of the capacitor discharge resembles a underdamped LRC oscillator. The current going through the pinch, $I_p$, was taken at $t = 11$ μs.

anodes and capacitors. A representative trace of the current waveform measured in this manner is detailed in Fig. 8.

Although the device current is convenient to measure, the $I_p$ that is referenced in Eq. (3) is the amount of current flowing through the pinch. Past studies [25] have investigated the spatial and temporal distribution of current within the deflagration accelerator and concluded that both effects are important to consider. It was found that virtually all of the current for much of the first positive half-period of the underdamped LRC oscillation is collected by the cathode within the accelerator volume and used to induce a B-field to accelerate the plasma. By the time the plasma has reached the end of the accelerator volume, the vast majority of the current flows directly through the concentrated area occupied by the pinch. Thus as with the estimates of characteristic length scales, a time of 11 μs after initial gas breakdown was used to obtain $I_p$, as marked in Fig. 8.

The resulting pinch properties calculated using the equilibrium model are detailed in Fig. 9. These properties and specifically of note, the pressure profile, indicate the magnitude and structure required to maintain a stable pinch. The spatial scale shown in Fig. 9 is a reflection of the measured density profiles which feature characteristic radii comparable to the time-resolved gradient length scales measured with the Schlieren diagnostic. Calculations made using the model are also consistent in both structure, trend, and value with surface mounted magnetic probe and Thomson scattering measurements for $B$ and $T$ respectively for a similar device in Refs. [24,26].

## 4. Astrophysical scaling

It is important to establish both device parameters and to calculate relevant dimensionless numbers for laboratory astrophysics experiments. The experimental measurements presented in this work were used to quantify the plasma jet properties. Namely, Stark broadening was used to measure the density, time of flight was used to measure velocity, Schlieren imaging was used to measure gradient length scales and the pinch model was used to obtain both the plasma's magnetic field and temperature. From these properties, a number of other quantities can be calculated that are relevant to magnetohydrodynamic flows.

A number of studies have investigated the scaling and similarity properties of the governing plasma fluid equations by establishing dimensionless groups. Some research such as Ref. [30] include additional physics to account for optical depth effects of the plasma. As

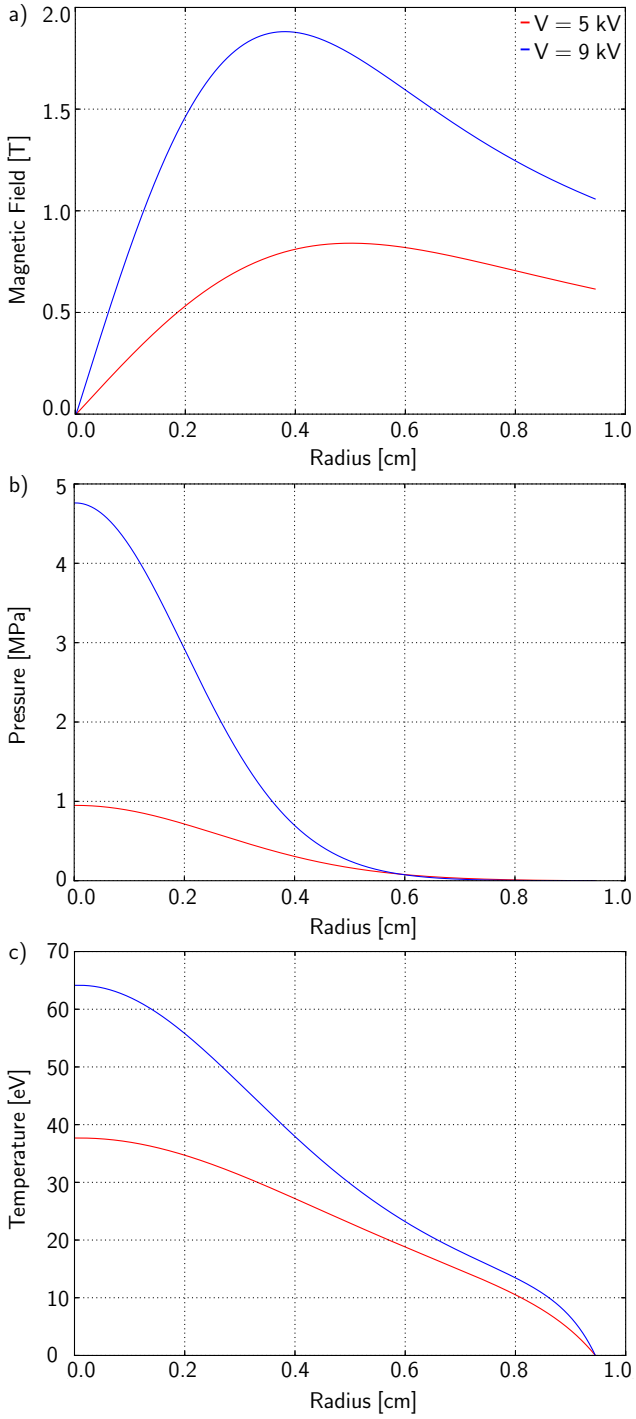


**Fig. 9.** Plots of the pinch properties as a function of radius derived from the equilibrium model: (a) magnetic field, (b) pressure, and (c) temperature. Note the pressure here is the equilibrium pinch pressure and not the ram pressure of the jet.

there are so many different similarity variables for virtually any astrophysical body, there are no laboratory experiments that can claim to recreate all essential physics. Thus in many cases, the suitability of a laboratory experiment is instead determined by its ability to recreate specific physics of interest. Three dimensionless groups that are universally cited as important metrics for establishing the similarity between astrophysical and laboratory systems are the Reynolds number, Re, magnetic Reynolds number, $\mathrm{Re}_m$, and Euler number, Eu,

**Table 1**
Characteristic scales and dimensionless parameters for a variety of astrophysical environments and laboratory scale experiments [28,29]. The properties specified for the deflagration accelerator were the maximum measured and $L^*$ was taken as the pinch radius.

| Environment | $L^*$ [m] | $V$ [m/s] | $n$ [m$^{-3}$] | $T$ [eV] | $B$ [T] | Re | Re$_m$ | Eu |
|---|---|---|---|---|---|---|---|---|
| Warm ISM | $3\times10^{16}$ | $10^5$ | $10^6$ | 1 | $10^{-9}$ | $10^7$ | $10^{19}$ | 10 |
| Dense cloud | $3\times10^{16}$ | $5\times10^3$ | $10^9$ | $10^{-2}$ | $10^{-8}$ | $7\times10^{13}$ | $6\times10^{14}$ | 6 |
| Stellar atmosphere | $10^7$ | $10^5$ | $10^{21}$ | 1 | $10^{-2}$ | $5\times10^{12}$ | $4\times10^9$ | 10 |
| AGN disk | $2\times10^{11}$ | $3\times10^6$ | $10^{18}$ | $10^3$ | $10^2$ | $7\times10^7$ | $6\times10^{13}$ | 10 |
| XRB disk | $10^4$ | $3\times10^5$ | $3\times10^{27}$ | $10^3$ | $10^2$ | $10^9$ | $4\times10^{11}$ | 1 |
| Omega Hohlraum | $10^{-4}$ | $10^5$ | $10^{28}$ | $10^2$ | $10^2$ | $3\times10^3$ | $5\times10^1$ | 1 |
| NIF Hohlraum | $3\times10^{-4}$ | $2\times10^5$ | $10^{28}$ | $3\times10^2$ | $10^2$ | $10^3$ | $2\times10^3$ | 1 |
| Z experiment | $10^{-3}$ | $10^5$ | $10^{28}$ | $10^2$ | $10^2$ | $3\times10^4$ | $5\times10^2$ | 1 |
| Short pulse laser | $10^{-5}$ | $10^6$ | $10^{30}$ | $10^3$ | $10^4$ | $10^3$ | $10^3$ | 4 |
| Wire Z-Pinch [27] | $10^{-3}$ | $10^5$ | $10^{24}$ | $10^2$ | $\sim 50$ | $10^4$ | 10 | 1 |
| Deflagration accel. | $4\times10^{-3}$ | $10^5$ | $10^{23}$ | $6\times10^1$ | 2 | 10 | $2\times10^2$ | 1 |

$$\mathrm{Re} = \frac{VL}{\nu}, \tag{7}$$

$$\mathrm{Re}_m = VL\mu_0\sigma, \tag{8}$$

$$\mathrm{Eu} = V\sqrt{\frac{\rho}{p}}. \tag{9}$$

Within these expressions, $V$ refers to the jet velocity, $L$ is the characteristic length scale in the flow, $\nu$ is the plasma kinematic viscosity and $\sigma$ is the conductivity. Expressions for both $\nu$ and the plasma resistivity, $\eta$, are given in Refs. [31,32] as,

$$\nu[\mathrm{m^2\ s^{-1}}] = \mathrm{Min}\begin{cases} 3.3\times10^{-6}\dfrac{\sqrt{A}[T(\mathrm{eV})]^{5/2}}{\Lambda Z^4\rho(\mathrm{kg\ m^{-3}})}, \\ \dfrac{2\alpha T(\mathrm{eV})}{ZB(\mathrm{T})} \end{cases} \tag{10}$$

$$\eta_\perp[\Omega\ \mathrm{m}] = 1.96\eta_\parallel = 1.039\times10^{-4}\frac{Z\Lambda}{T_e^{3/2}(\mathrm{eV})}. \tag{11}$$

where the plasma resistivity is related to the conductivity by $\eta = 1/\sigma$. Within the equation for $\nu$, two different formulas are presented where in one the effect of a magnetic field is neglected and the second it is taken into account. As detailed in Ref. [31], the minimum of the two is taken as the plasma viscosity. Remaining terms in Eqs. (10) and (11) include, the Coulomb logarithm ($\Lambda \approx 10$), the ion atomic mass number, $A$, and magnetic field entanglement parameter, $\alpha$. In Eq. (11), it was further assumed that the current flow in the pinch is normal to the self-generated magnetic field.

The measured characteristic parameters for the deflagration accelerator along with a variety of other experimental platforms and astrophysical flows is detailed in Table 1. The pinch radius was chosen as the characteristic length scale in evaluation of all dimensionless numbers. Compared to many of the laser experiments, our device offers a larger characteristic length scale, similar velocity/temperature, but lower plasma density and magnetic field. However, the deflagration jet offers significant advantages in lifetime (over 1000 times longer than those summarized in Refs. [33,34]) and both radial and axial extent, as shown in Table 2. These features allow the accelerator to offer a unique ability to study dynamics and instabilities with longer timescales.

In terms of dimensionless numbers, the scale between experiments and astrophysical flows is large. In many cases for validation of numerical codes and testing of physics, it is sufficient to ensure the regime of the governing equations is maintained between systems. As nearly all astrophysical flows of interest, and all of those shown in Table 1, feature both large Re and Re$_m$, an important determination is if a given experiment can maintain the ideal magnetohydrodynamic constraints, Re $\gg$ 1 and Re$_m$ $\gg$ 1. In terms of the magnetic Reynolds number, our experiment maintains the requirement that Re$_m$ $\gg$ 1 implying that flux lines of the magnetic field are advected by the resulting flow. The other constraint is not strictly met as Re $\approx$ 10 implying that viscous effects might be important, however it is still an order of magnitude above unity. The applicability of the experiment for simulating specific physics not considered directly in this paper can be answered by taking the experimental parameters in Table 1 and evaluating the appropriate dimensionless group of interest.

**Table 2**
Comparison of critical length and temporal scales for the laser produced jets [33,34] and those from the device considered in this work.

| Quantity | Laser | Deflagration |
|---|---|---|
| Jet length [m] | $5\times10^{-3}$ | $6\times10^{-2}$ |
| Jet radius [m] | $1.5\times10^{-4}$ | $4\times10^{-3}$ |
| Time scale [s] | $2\times10^{-9}$ | $10^{-5}$ |

## 5. Conclusion

This work has presented an experimental characterization of a novel device in the context of astrophysical flows. The deflagration accelerator boasts enormous advantages of inexpensive upkeep, high repeatability, and nearly unprecedented diagnostic access compared to conventional laser facilities. This ease of access allows for systematic studies of not only the properties of astrophysical jets but also their interaction with neutral gases. Perhaps the most unique application is the device's ability to study jet stability, formation and interaction in a truly spatial and time-resolved manner while still retaining appropriate scaling to astrophysical environments. With jets that last ~10 μs, state of the art continuous framing cameras (10 million frames per second) can be used with the accelerator to take videos of astrophysical flows. Such studies would not be possible with other devices featuring characteristic timescales in the nanoseconds as only a handful of images would be captured. Beyond that, the device removes practical issues such as target fabrication while incorporating essential physics in that the produced jet is completely driven by internal current flow and resulting induced magnetic fields. With the measured similarity parameters and ability to study time-resolved phenomena including instability dynamics and plasma interactions, this experimental platform is well suited to investigate contemporary astrophysical problems.

## Acknowledgments

This work is supported by the U.S. Department of Energy Grant No. DE-NA0002011. The authors also want to thank Hadland

Imaging for graciously letting them borrow the camera utilized in this work and Dr. Vic Miller for his assistance with setting up the Schlieren imaging experiment. Thomas Underwood and Keith Loebner also gratefully acknowledge the financial support of the National Defense Science and Engineering Graduate Fellowship Program.

## References

[1] B. Balick, A. Frank, Shapes and shaping of planetary nebulae, Annu. Rev. Astron. Astrophys. 40 (1) (2002) 439–486, doi: 10.1146/annurev.astro.40.060401.093849.
[2] B. Reipurth, J. Bally, Herbig-haro flows: probes of early stellar evolution, Annu. Rev. Astron. Astrophys. 39 (1) (2001) 403–455, doi: 10.1146/annurev.astro.39.1.403.
[3] K.J. Borkowski, J.M. Blondin, J.P. Harrington, Collimation of astrophysical jets: the proto-planetary nebula he 3−1475, Astrophys. J. Lett. 482 (1) (1997) L97. URL: http://stacks.iop.org/1538-4357/482/i=1/a=L97
[4] G. Gregori, B. Reville, F. Miniati, The generation and amplification of intergalactic magnetic fields in analogue laboratory experiments with high power lasers, Phys. Rep. 601 (2015) 1–34, doi: 10.1016/j.physrep.2015.10.002. The generation and amplification of intergalactic magnetic fields in analogue laboratory experiments with high power lasers, URL: http://www.sciencedirect.com/science/article/pii/S0370157315004317
[5] B. Albertazzi, A. Ciardi, M. Nakatsutsumi, T. Vinci, J. Béard, R. Bonito, J. Billette, M. Borghesi, Z. Burkley, S.N. Chen, T.E. Cowan, T. Herrmannsdörfer, D.P. Higginson, F. Kroll, S.A. Pikuz, K. Naughton, L. Romagnani, C. Riconda, G. Revet, R. Riquier, H.-P. Schlenvoigt, I.Y. Skobelev, A. Faenov, A. Soloviev, M. Huarte-Espinosa, A. Frank, O. Portugall, H. Pépin, J. Fuchs, Laboratory formation of a scaled protostellar jet by coaligned poloidal magnetic field, Science 346 (6207) (2014) 325–328, doi: 10.1126/science.1259694. URL: http://science.sciencemag.org/content/346/6207/325
[6] J.M. Foster, B.H. Wilde, P.A. Rosen, R.J.R. Williams, B.E. Blue, R.F. Coker, R.P. Drake, A. Frank, P.A. Keiter, A.M. Khokhlov, J.P. Knauer, T.S. Perry, High-energy-density laboratory astrophysics studies of jets and bow shocks, Astrophys. J. Lett. 634 (1) (2005) L77. URL: http://stacks.iop.org/1538-4357/634/i=1/a=L77
[7] S.V. Lebedev, J.P. Chittenden, F.N. Beg, S.N. Bland, A. Ciardi, D. Ampleford, S. Hughes, M.G. Haines, A. Frank, E.G. Blackman, T. Gardiner, Laboratory astrophysics and collimated stellar outflows: the production of radiatively cooled hypersonic plasma jets, Astrophys. J. 564 (1) (2002) 113. URL: http://stacks.iop.org/0004-637X/564/i=1/a=113
[8] F. Suzuki-Vidal, S. Lebedev, M. Krishnan, J. Skidmore, G. Swadling, M. Bocchi, A. Harvey-Thompson, S. Patankar, G. Burdiak, P. de Grouchy, L. Pickworth, S. Stafford, L. Suttle, M. Bennett, S. Bland, J. Chittenden, G. Hall, E. Khoory, R. Smith, A. Ciardi, A. Frank, R. Madden, K. Wilson-Elliot, P. Coleman, Interaction of radiatively cooled plasma jets with neutral gases forlaboratory astrophysics studies, High Energy Density Phys. 9 (1) (2013) 141–147, doi: 10.1016/j.hedp.2012.11.003. URL: http://www.sciencedirect.com/science/article/pii/S1574181812001292
[9] H. Baty, R. Keppens, Interplay between kelvin-helmholtz and current-driven instabilities in jets, Astrophys. J. 580 (2) (2002) 800. URL: http://stacks.iop.org/0004-637X/580/i=2/a=800
[10] S. Appl, T. Lery, H. Baty, Current-driven instabilities in astrophysical jets. linear analysis, Astron. Astrophys. 355 (2000) 818–828.
[11] T. Lery, H. Baty, S. Appl, Current-driven instabilities in astrophysical jets. Non linear development, Astron. Astrophys. 355 (2000) 1201–1208.
[12] J. Marshall, Performance of a hydromagnetic plasma gun, Phys. Fluids 3 (1) (1960) 134–135, doi: 10.1063/1.1705989. URL: http://scitation.aip.org/content/aip/journal/pof1/3/1/10.1063/1.1705989
[13] D.Y. Cheng, P. Wang, Experimental observation of the high-density plasma-beam formation by continuous-flow z-pinch, Nucl. Fusion 13 (3) (1973) 458. URL: http://stacks.iop.org/0029-5515/13/i=3/a=018
[14] D.M. Woodall, L.K. Len, Observation of current sheath transition from snowplow to deflagration, J. Appl. Phys. 57 (3) (1985) 961–964, doi: 10.1063/1.334697. URL: http://scitation.aip.org/content/aip/journal/jap/57/3/10.1063/1.334697
[15] K.T. Loebner, T.C. Underwood, B.C. Wang, M.A. Cappelli, Damage morphologies in targets exposed to a new plasma deflagration accelerator for ELM simulation, IEEE Trans. Plasma Sci. (2016). URL: http://scitation.aip.org/content/aip/journal/rsi/86/6/10.1063/1.4922522
[16] U. Shumlak, B. Nelson, B. Balick, Plasma Jet Studies via the Flow Z-Pinch, Springer, Netherlands, 2007, doi: 10.1103/PhysRevLett.75.3285.
[17] K.T.K. Loebner, T.C. Underwood, M.A. Cappelli, A fast rise-rate, adjustable-mass-bit gas puff valve for energetic pulsed plasma experiments, Rev. Sci. Instrum. 86 (6) (2015), doi: 10.1063/1.4922522.
[18] K.T.K. Loebner, T.C. Underwood, M.A. Cappelli, Evidence of branching phenomena in current-driven ionization waves, Phys. Rev. Lett. 115 (2015) 175001, doi: 10.1103/PhysRevLett.115.175001.
[19] U. Shumlak, C.W. Hartman, Sheared flow stabilization of the $m = 1$ kink mode in $Z$ pinches, Phys. Rev. Lett. 75 (1995) 3285–3288, doi: 10.1103/PhysRevLett.75.3285.
[20] K.T.K. Loebner, B.C. Wang, F.R. Poehlmann, Y. Watanabe, M.A. Cappelli, High-velocity neutral plasma jet formed by dense plasma deflagration, IEEE Trans. Plasma Sci. 42 (10) (2014) 2500–2501, doi: 10.1109/TPS.2014.2332467.
[21] O.H. Nestor, H.N. Olsen, Numerical methods for reducing line and surface probe data, SIAM Rev. 2 (3) (1960) 200–207, doi: 10.1137/1002042.
[22] H. Ehrich, D.E. Kelleher, Experimental investigation of plasma-broadened hydrogen balmer lines at low electron densities, Phys. Rev. A 21 (1980) 319–334, doi: 10.1103/PhysRevA.21.319.
[23] G. Settles, Schlieren and Shadowgraph Techniques: Visualizing Phenomenon in Transparent Media, second ed., Springer, 2006.
[24] S.L. Jackson, Density Characteristics of a Sheared-Flow Z-Pinch, University of Washington, 2006 Ph.D. thesis.
[25] F.R. Poehlmann, M.A. Cappelli, G.B. Rieker, Current distribution measurements inside an electromagnetic plasma gun operated in a gas-puff mode, Phys. Plasmas 17 (12) (2010), doi: 10.1063/1.3526603. URL: http://scitation.aip.org/content/aip/journal/pop/17/12/10.1063/1.3526603
[26] U. Shumlak, R.P. Golingo, B.A. Nelson, D.J. Den Hartog, Evidence of stabilization in the $Z$-pinch, Phys. Rev. Lett. 87 (2001) 205005, doi: 10.1103/PhysRevLett.87.205005. URL: http://link.aps.org/doi/10.1103/PhysRevLett.87.205005
[27] S.V. Lebedev, A. Ciardi, D.J. Ampleford, S.N. Bland, S.C. Bott, J.P. Chittenden, G.N. Hall, J. Rapley, C.A. Jennings, A. Frank, E.G. Blackman, T. Lery, Magnetic tower outflows from a radial wire array z-pinch, Mon. Not. R. Astron. Soc. 361 (1) (2005) 97–108, doi: 10.1111/j.1365-2966.2005.09132.x.
[28] P. Babington, Jets from Young Stars IV, first ed., 793, Springer-Verlag, Berlin Heidelberg, 2010.
[29] J.I. Castor, Astrophysical Radiation Dynamics: The Prospects for Scaling, Springer Netherlands, Dordrecht, 2007, doi: 10.1007/978-1-4020-6055-7_38.
[30] J.E. Cross, B. Reville, G. Gregori, Scaling of magneto-quantum-radiative hydrodynamic equations: from laser-produced plasmas to astrophysics, Astrophys. J. 795 (1) (2014) 59.
[31] D. Ryutov, R.P. Drake, J. Kane, E. Liang, B.A. Remington, W.M. Wood-Vasey, Similarity criteria for the laboratory simulation of supernova hydrodynamics, Astrophys. J. 518 (2) (1999) 821. URL: http://stacks.iop.org/0004-637X/795/i=1/a=59
[32] M. Mitchner, C. Kruger, Partially Ionized Gases, John Wiley and Sons, 1992.
[33] V.T. Tikhonchuk, P. Nicolai, X. Ribeyre, C. Stenz, G. Schurtz, A. Kasperczuk, T. Pisarczyk, L. Juha, E. Krousky, K. Masek, M. Pfeifer, K. Rohlena, J. Skala, J. Ullschmied, M. Kalal, D. Klir, J. Kravarik, P. Kubes, P. Pisarczyk, Laboratory modeling of supersonic radiative jets propagation in plasmas and their scaling to astrophysical conditions, Plasma Phys. Control. Fusion 50 (12) (2008) 124056. URL: http://stacks.iop.org/0004-637X/518/i=2/a=821
[34] D.R. Farley, K.G. Estabrook, S.G. Glendinning, S.H. Glenzer, B.A. Remington, K. Shigemori, J.M. Stone, R.J. Wallace, G.B. Zimmerman, J.A. Harte, Radiative jet experiments of astrophysical interest using intense lasers, Phys. Rev. Lett. 83 (1999) 1982–1985, doi: 10.1103/PhysRevLett.83.1982. URL: http://link.aps.org/doi/10.1103/PhysRevLett.83.1982